Arabian Journal of Chemistry (2022) **15**, 104256

King Saud University

**Arabian Journal of Chemistry**

www.ksu.edu.sa
www.sciencedirect.com

ORIGINAL ARTICLE

# Role of rhodium doping into lanthanum cobalt oxide ($LaCoO_3$) perovskite and the induced bifunctional activity of oxygen evolution and reduction reactions in alkaline medium

**Mohamed A. Ghanem [a,*], Mabrook S. Amer [a,b], Prabhakarn Arunachalam [a], Abdullah M. Al-Mayouf [a,b], Mark T. Weller [c]**

[a] *Chemistry Department, King Saud University, Riyadh 11451, Saudi Arabia*
[b] *K. A. CARE Energy Research and Innovation Centre at Riyadh, Riyadh, Saudi Arabia*
[c] *Chemistry Department, Cardiff University, Cardiff CF10 3AT, UK*

Received 9 June 2022; accepted 10 September 2022
Available online 16 September 2022

**KEYWORDS**

Lanthanum cobalt oxide;
Perovskites;
Rhodium;
Oxygen evolution and reduction reactions

**Abstract** Transition metal oxides, especially perovskites, have been considered effective electrocatalysts for the oxygen evolution (OER) and oxygen reduction (ORR) reactions in an alkaline solution. Here, a series of lanthanum cobalt rhodium oxide perovskites with the chemical formula $LaCo_{1-x}Rh_xO_3$ (LCRO, $0.1 \leq x \leq 0.70$) were prepared through the approach of solid-phase synthesis and their bifunctional electrocatalytic activity was assessed for both the OER and ORR. The crystallinity, morphology, surface, and electrocatalytic features of the LCRO were significantly correlated with the rhodium content. The $LaCo_{0.7}Rh_{0.3}O_3$ electrocatalysts with $x = 0.3$ showed enhanced electrocatalytic bifunctional performance with a substantially lower OER/ORR onset potential of 1.38/0.73 V vs HRE, smaller Tafel slope (116/90 mV/dec), and low charge-transfer resistance, which is the most efficient catalyst among the other studied ratios and superior to the pristine lanthanum cobalt oxide benchmark electrocatalysts. The $LaCo_{0.7}Rh_{0.3}O_3$ electrode exhibit good bifunctional electrocatalytic behavior and long-term durability with an OER and ORR onset potential gap ($\Delta E = E_{OER} - E_{ORR}$) of only 0.65 V, which could be credited to the enriched oxygen vacancies, lattice expansion and the improved electrical conductivity upon the doping of larger size

* Corresponding authors.
E-mail address: mghanem@ksu.edu.sa (M.A. Ghanem).
Peer review under responsibility of King Saud University.

Production and hosting by Elsevier

https://doi.org/10.1016/j.arabjc.2022.104256

of Rh ions. The $LaCo_{1-x}Rh_xO_3$ catalysts are obtained from abundant materials that have the potential of highly-active bifunctional OER and ORR electrocatalysts.



## 1. Introduction

During the past years, electrochemical water-splitting has been an active research area for the production of hydrogen fuel for cleaner energy (Lee et al., 2022; Marini et al., 2012). Alkaline water electrolysis involves the reaction of oxygen evolution (OER, $4OH^- \rightarrow O_2 + 2H_2O + 4e^-$), which is a kinetically sluggish reaction owing to the proton-coupled multi-electron transfer process and the requirement for a large overpotential (Wang et al., 2016; Debe, 2012). Further, the reaction of oxygen reduction (ORR, $O_2 + 2H_2O + 4e^- \rightarrow 4OH^-$) is another electrochemical process for energy storage devices and fuel cells (Feng et al., 2018; Shahid et al., 2017). The development of economic, highly active catalysts for oxygen redox reactions for application in direct solar and electrochemical water electrolysis and metal-air batteries is considered the most technical task in energy technology (Xia et al., 2016). Therefore, there has been growing interest in developing and preparing non-precious metal catalytic materials that are highly efficient to replace the precious- and rare-metal-based electrocatalysts (Cheng et al., 2013; Chen et al., 2011; Wu et al., 2013)and to improve the overall activity and kinetics of the ORR and OER (Dou et al. 2020).

Perovskite-based oxides ($ABO_3$) are of considerable interest for creating next-generation catalytic materials, providing enriched bifunctional (OER) and (ORR) (Suntivich et al., 2011; Dias et al., 2020) electrocatalytic activity, and possessing benefits over precious-metal-based catalysts in terms of production cost and high durability at high temperature (Matsumoto et al., 1977; Bockris and Otagawa,1984; Kobussen and Broers, 1981; Matsumoto and Sato, 1980). Moreover, their rich composition variant, crystal structure, and morphology allow further tuning of their electronic and electrocatalytic activities for enhanced catalytic performance for the OER and ORR (Tanaka and Misono, 2001; Harris, 1970; Cui et al., 2021). Among the available catalysts, lanthanum-based perovskites, such as $LaCoO_3$, $LaNiO_3$, $LaCrO_3$, $LaMnO_3$, and $LaFeO_3$, have been extensively investigated for various electrochemical energy reactions owing to their structural stability, high electronic and ionic conductivities, and the capacity to fully or partially replace the cation of A-, B-site elements as well as the anion at the O-site to engineer the structural, physical, and electronic properties (Dias et al., 2020, Zhu et al., 2015; Celorrio et al., 2015; Petrie et al., 2016; Mefford et al., 2016). The full or partial substitution of $ABO_3$ perovskites leads to the weakening of the metal–oxygen bond and improves the B—O bond covalency, oxygen defects, and redox surface-active oxygen species, thus enhancing the electronic and ionic conductivity as well as the ORR and OER electrocatalytic activity (Dong et al., 2021; Xu et al., 2020; Zhang et al., 2020; Zhu et al., 2016). Within this context, the iron (Kim, et al., 2019) or nickel (Liu et al., 2019) doping in cobalt-based perovskites improves the ORR electrochemical activity in solid oxide fuel cell reaction. Moreover, the partial exchanging of the O-sites in the structure of $ABO_3$ perovskite with anions of $Br^-$, $Cl^-$ and $F^-$ (Ghanem et al., 2021, 2016; Zhang et al., 2020), $N^{3-}$ or $S^{2-}$ (Liu et al., 2019) significantly weakens the metal–oxygen bond, and consequently promotes the lattice oxygen activity and diffusion (Zhang et al., 2020). The oxygen vacancy concentration on the perovskite structure is found to have a pronounced effect on oxygen mobility as well as catalytic activity and selectivity. For instance, the exchange of Sr for La at the A site and the substitution of Co for Fe at the B site in $ABO_3$ perovskites have shown dramatic increases in the oxygen diffusion rate, which improves the overall activity of the water oxidation reaction (Chang et al., 2020). Furthermore, the *Ab initio* and DFT modeling have shown that the alkaline water electrolysis activity of $LaCoO_3$ can be enhanced by tuning the Co—O bond covalency and the oxygen vacancy concentration via partial $Sr^{2+}$ substitution (Mefford et al., 2016). The results demonstrated that in alkaline media the OER was significantly enhanced due to the increase of oxygen vacancies, which modulated the Fermi energy of the overlapped transition metal-3d and oxygen-2p orbitals. In addition, the $e_g$ filling factor of the B-metal in the $ABO_3$ perovskite has been shown to control the intermediate species binding energy, and consequently, significant perovskite water oxidation activity can be gained (Suntivich et al., 2011). The recent works have reported significant enhancement of the bifunctional OER and ORR performances of strontium iron and cobalt perovskites by partial doping with halide anions, with the activity increasing in the order Br < Cl < F (Liu et al., 2019; Ghanem et al., 2021, 2016). Herein and for the first time, we report the intrinsic bifunctional OER and ORR activities of a series of lanthanum cobalt oxides partially substituted by rhodium, $LaCo_{1-x}Rh_xO_3$ (LCRO, x = 0.1, 0.15, 0.20, 0.30, 0.40, 0.60, and 0.70). The effect of rhodium doping on the lanthanum cobalt oxide crystal structure, surface morphology, and oxygen vacancy concentration was investigated by diffractive X-ray, scanning electron microscopy (SEM), energy-dispersive X-ray (EDX) mapping, and X-ray photoelectron spectroscopy (XPS). The OER and ORR bifunctional electrochemical activity of LCRO in alkaline solution were significantly correlated with the Rh content and the $LaCo_{0.7}Rh_{0.3}O_3$ electrode materials with x = 0.3 showed enhanced electrocatalytic performance with a significant negative shift (170 mV) in the OER onset potential, Tafel slope of 116 mV/dec, ultra-low charge-transfer resistance, and current density of 104.2 mA $cm^{-2}$ at 1.6 $V_{RHE}$, which is a more active catalyst than other investigated Rh-doped ratios. Based on the electrochemical measurements, the $LaCo_{0.7}Rh_{0.3}O_3$ electrocatalyst was very stable during the prolonged OER and ORR process in an alkaline medium. This work explores the controlled chemical modifications/-doping of a new set of 3d-4d transition metals of Co and Rh within the LCRO perovskite while maintaining the crystal structure and enabling monitoring of the effects of the covalency and oxygen vacancy concentration on the bifunctional OER and ORR activity.

## 2. Experimental

### 2.1. Materials preparation and synthesis

Lanthanum cobalt rhodium perovskite oxides (LCRO) with nominal composition of $LaCo_{1-x}Rh_xO_3$ (x = 0.1, 0.15, 0.20, 0.30, 0.40, 0.60, and 0.7) were prepared using a standard high-temperature solid-state reaction method. Mixtures of $La_2O_3$ (99.95 %, Sigma-Aldrich), $Co_3O_4$ (99.9 %, Sigma-Aldrich), and $Rh_2O_3$ (99.99 %, Johnson-Matthey) with the various target product stoichiometric molar ratios were ground together in an agate pestle and mortar, placed in a platinum crucible, and heated to 1150 °C in air. The partly reacted product was reground, pressed into a pellet, and sintered for two further periods of 48 h at 1150 °C in air. The catalysts then were left to cool at room temperature, ground, and stored in a desiccator for further characterization.

### 2.2. Catalysts characterizations

The phase structures of the obtained samples were investigated using X-ray diffraction (XRD, Rigaku Miniflex 600, Rigaku

Corporation, Tokyo, Japan). The XRD results were obtained within the 2Θ range of 5–80° with 0.02° step and a scan speed of 10° $min^{-1}$ and operated voltage and current of 40 kV and 15 mA respectively. The Rietveld refinement method was used to obtain the space group and the crystalline parameters from the XRD data. The catalyst morphologies and elemental compositions of the synthesized catalysts were examined by SEM (S-4800, Hitachi) fitted with an EDX spectrometer (EX350, Horiba). X-ray photoelectron spectroscopic analysis of the produced materials was achieved using the spectrometer of Escalab 250 XPS (Thermo Fisher).

### *2.3. Catalyst electrodes synthesis and electrochemical measurements*

Electrochemical characterizations were evaluated at room temperature using a three-electrode cell connected to an electrochemical Bio-Logic two-channel potentiostat (VMP3). The catalyst ink was physically cast onto an electrode of carbon paper (CP, SIGRACET® GDL-24BC, area of 1.0 × 1.0 c $m^2$), which was employed as the working electrode, and a high-purity graphite sheet (1.0 × 1.0 × 0.3 $cm^3$) electrode and the saturated calomel electrode (SCE) were employed as the auxiliary and reference electrodes, respectively. The electrode potential was normalized to the hydrogen reference electrode (RHE) using the equation of $E_{(RHE)} = E_{(SCE)} + 0.243 + 0.059pH$. The CP electrode was pre-activated in hot concentrated $HNO_3$ for 40 *sec* followed by rinsing with deionized water and drying before catalyst casting. The ink of the $LaCo_{1-x}Rh_xO_3$ catalysts was prepared by dispersing 10 mg of catalyst powder in 1.0 ml of water: isopropanol solution (volume ratio of 0.5:0.5), and then 10 µl of Nafion solution was added. The mixture was sonicated for 30 min to generate a homogeneous electrocatalyst ink. Finally, 60 µl of as-prepared catalyst ink was coated on the surface of the CP electrode, resulting in an approximate catalyst loading of 0.6 mg/$cm^2$. The OER and ORR were investigated in an aqueous solution of 1.0 M KOH (pH 13.8) and before each experiment, $N_2$ gas was purged through the KOH electrolyte for 30 min to remove the dissolved oxygen. The electrochemical measurement of the ORR activity was performed in a 0.1 M KOH aqueous solution using a rotating ring-disk electrode (RRDE, make, and supply) comprising a glassy carbon disk and a platinum ring electrode. To prepare the catalyst dispersion, 10.0 mg of the investigated catalyst was dispersed in 1.0 ml of water: isopropanol solution (volume ratio of 0.5:0.5), and then 10 µl of Nafion solution was added. The $H_2O_2$ yield and the number of transferred electrons ($n$) during the ORR over the oxyhalide catalyst were calculated using equations (1) and (2), respectively.

$$H_2O_2\% = (200\ I_r/N)/(I_d + I_r/N) \quad (1)$$

$$n = (4I_d)/(I_d + I_r/N) \quad (2)$$

where $N$ is the current collection efficiency, $I_r$ is the ring current and $I_d$ is the disk current of the RRDE.

## 3. Results and discussion

### *3.1. Characterizations of the $LaCo_{1-x}Rh_xO_3$ catalysts*

the XRD patterns of the $LaCo_{1-x}Rh_xO_3$ catalysts doped with different ratios of Rh are shown in Fig. 1. The obtained catalysts are highly crystalline with the main diffraction peaks at 2θ of 23.10, 32.74, 40.32, 47.06, 53.01, 58.35, 68.7, and 78.22 consistent with the (012), (110), (202), (024), (116), (300),

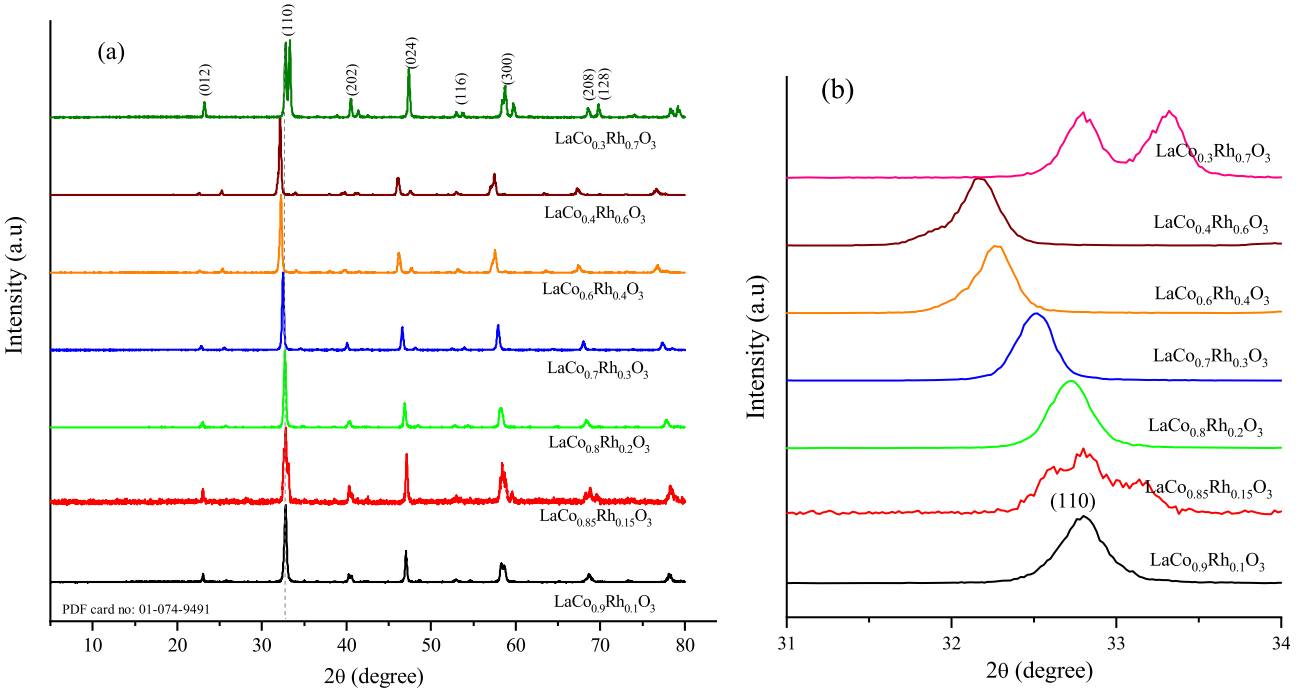


**Fig. 1** (a) XRD patterns of as-prepared $LaCo_{1-x}Rh_xO_3$ perovskite catalysts with different doped Rh ratios prepared by solid-state reactions are indexed using reference peak (PDF # 01-074-9491), (b) the corresponding enlarged view of the (110) diffraction plane.

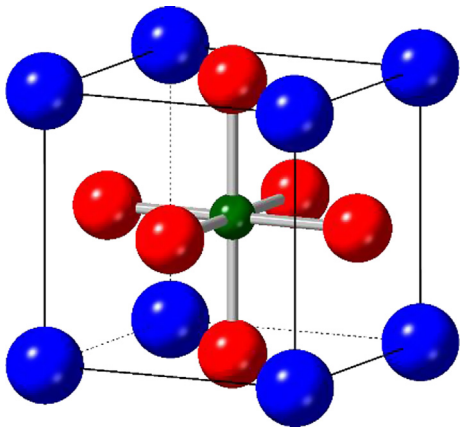

**Scheme 1** The perovskite structure of $LaCo_{1-x}Rh_xO_3$ is adopted for the majority of × values. La blue, oxygen red, and Co/Rh dark green.

(2 0 8), and (1 2 8) diffraction planes, respectively (PDF card no: 01–074-9491). Moreover, the cubic perovskite structure adopted by the majority of these $LaCo_{1-x}Rh_xO_3$ catalysts is shown in Fig. 1. The $LaCo_{1-x}Rh_xO_3$ catalysts with x = 0.1, 0.20, 0.30, 0.40, and 0.60 have a single phase of cubic perovskite, as evidenced by the single uniform diffraction peak of the (1 1 0) crystal plane at 2θ = 32.74, shown in Scheme 1. For x = 0.15, i.e., $LaCo_{0.85}Rh_{0.15}O_3$, a perovskite structure type was identified through the breadth of the reflections, as shown in Fig. 1b (red line), which indicates a degree of phase separation for this composition or distortion of the perovskite structure to a lower symmetry ($GdFeO_3$ structure type). However, for x = 0.7, i.e., $LaCo_{0.3}Rh_{0.7}O_3$, a single perovskite phase material was not formed, and the PXD pattern indicated phase separation into two perovskites with compositions $LaRhO_3$ ($GdFeO_3$ structure type) and $LaCo_{0.85}Rh_{0.15}O_3$. The shift of the reflections to the lower 2θ as the level of rhodium increases represents the expansion of the unit cell as $Rh^{3+}$ replaces $Co^{3+}$ with the lattice parameter expanding from 3.876(2) Å ($LaCo_{0.9}Rh_{0.1}O_3$) to 3.914(2) Å ($LaCo_{0.4}Rh_{0.6}O_3$) indicating on the weakening of the B—O bond upon the Rh doping.

The surface morphological nature of the $LaCo_{1-x}Rh_xO_3$ catalysts with x = 0.1, 0.2, 0.3, and 0.4 was examined by SEM, as displayed in Fig. 2. The SEM micrographs in Fig. 2a and 2b show the LCRO catalyst at Co/Rh ratios of 0.1 and 0.2, respectively, have large, coarse, irregular particles with sizes of several micrometers. However, as shown in Fig. 2c and 2d, at Rh content of 0.3 and 0.4, the catalyst particles become more uniform and have a smoother surface with smaller particle sizes within the range of 1.0 to 3.0 μm. The dense oxide particles indicate that the catalysts are probably crystalline and free from pores, which is consistent with XRD results. However, the SEM microstructure characterization images show the presence of interstitial macropores between microparticles, which could facilitate the mass transport of the reactants and products during the electrochemical reactions.

The EDX composition mapping and elemental analysis of the $LaCo_{0.7}Rh_{0.3}O_3$ catalysts are shown in Fig. 3. In addition, Table 1 reports the EDX elemental composition analysis and the corresponding mole ratios for some samples of the $LaCo_{1-x}Rh_xO_3$ catalysts. The EDX mapping of the $LaCo_{0.7}Rh_{0.3}O_3$ catalyst discloses the existence of La, Co, Rh, and O components uniformly distributed throughout the sample (Fig. 3). Particularly, the EDX analysis of the $LaCo_{0.7}Rh_{0.3}O_3$ catalyst reveals the element wt.% of 55.48, 17.05, 10.58, and 16.89 for La, Co, Rh, and O elements, respectively, which corresponds to the chemical composition of $LaCo_{0.72}Rh_{0.31}O_{4.40}$, which is very close to the intended composition of the $LaCo_{0.7}Rh_{0.3}O_3$ catalyst. Moreover, Table S1 shows that the mole ratios of La, Co, Rh, and O obtained from EDX element composition analysis are in good agreement for the $LaCo_{1-x}Rh_xO_3$ catalysts with x = 0.1, 0.2, 0.3 and 0.7. From the EDX composition mapping and elemental analysis, we can conclude that La, Co, Rh, and O elements are homogeneously distributed throughout the $LaCo_{1-x}Rh_xO_3$ catalysts and their composition mole ratios match the intended stoichiometric compositions of the catalysts.

The effect of partial replacement of cobalt by rhodium on the surface functionality and oxygen vacancies of the $LaCo_{1-x}Rh_xO_3$ catalysts was examined by XPS. The wide survey and the narrow scan XPS spectra of the $LaCo_{0.9}Rh_{0.1}O_3$, $LaCo_{0.7}Rh_{0.3}O_3$, and $LaCo_{0.3}Rh_{0.7}O_3$ catalysts are shown in Fig. 4. The comparative XPS wide spectra of the $LaCo_{1-x}Rh_xO_3$ catalysts with x = 0.1, 0.3, and 0.7, as illustrated in Fig. 4a reveal the presence of La 3d, Co 2p, Rh 3d, and O 1s peaks. Moreover, a C 1s peak due to carbon surface contamination is regularly present. Fig. 4(b–d) shows the O 1s deconvoluted core spectra of $LaCo_{0.9}Rh_{0.1}O_3$, $LaCo_{0.7}Rh_{0.3}O_3$, and $LaCo_{0.3}Rh_{0.7}O_3$ catalysts, whereas Table 2 tabulates the binding energies (BE) of O 1s deconvoluted peaks and oxygen vacancy ratios for the $LaCo_{1-x}Rh_xO_3$ catalysts with x = 0.1, 0.3 and 0.7. In the asymmetrical O 1s, the core-level spectrum of the $LaCo_{0.9}Rh_{0.1}O_3$ catalyst (Fig. 4b) can be deconvoluted and assigned into two peaks of lattice $O^{2-}$ anion (1st peak) and $O^{1-}/O^{chem}$ (2nd peak), presumably because the quantity of chemisorbed oxygen species is too little. However, the asymmetrical O1s core-level spectra in Fig. 4c–d disclose the existence of a peak (3rd peak) at lower BE that can be assigned to the lattice oxygen of $O^{2-}$ anion of, while the peak in the middle is related to the surface $O^{1-}$ ions (2nd peak), and the peak 3 in at higher energy is related to the oxygen surface chemisorbed species ($O^{chem}$) (Dupin et al., 2000; Lemoine et al., 2019).

From the data in Table 2 and with an increasing ratio of rhodium, the overall peak BE of the $LaCo_{0.7}Rh_{0.3}O_3$ catalyst is shifted to lower BE compared to $LaCo_{0.9}Rh_{0.1}O_3$, which indicates weaker Co—O bonding because the withdrawal of the electron density away from the Co–atom, consequently enhancing the reactivity of lattice oxygen ($O^{2-}$) and decreasing the energy required for $O^{2-}$ activation.[32,33] Besides, the O 1s deconvoluted peak area ratios of $[O^{1-}/O^{2-}]$ as well as $[(O^{1-} + O^{chem})/O^{2-}]/O^{2-}]$ were much higher in the $LaCo_{0.7}Rh_{0.3}O_3$ catalyst (6.66, 8.17) than for the $LaCo_{0.3}Rh_{0.7}O_3$ (4.62, 3.25) and the $LaCo_{0.9}Rh_{0.1}O_3$ (6.66, 8.17) catalysts.

Finally, the doping of Rh ions into $LaCo_{1-x}Rh_xO_3$ at x = 0.3 enriched the $O^{1-}$ and $O^{chem}$ site concentration, which is directly associated with the surface oxygen vacancies and defects (Dupin et al., 2000; Lemoine et al., 2019). It has been widely reported that creating more oxygen vacancy concentration within the perovskite structure via doping/modifying the B site significantly enhances the catalytic activity by increasing the Co 3d/O 2p bands overlapping, B—O bond covalency, and

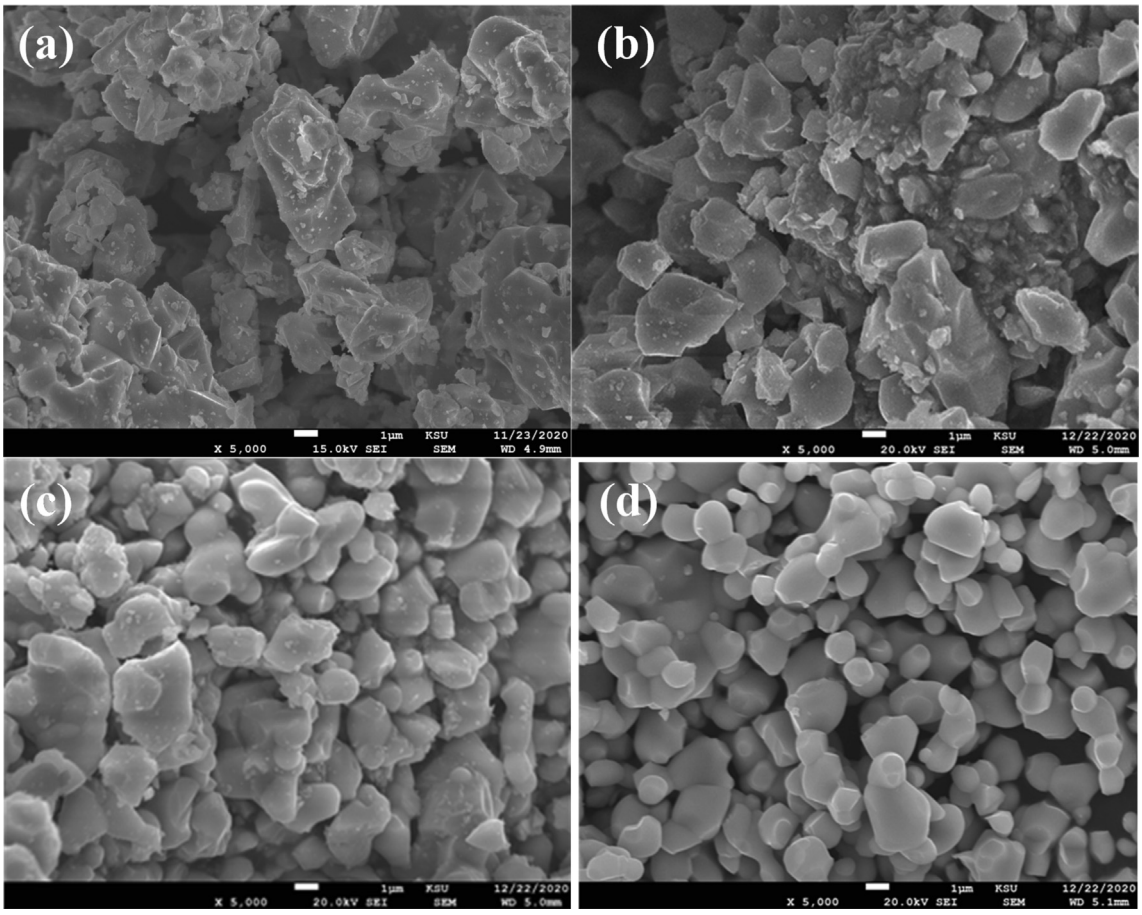


**Fig. 2** Morphological SEM characterization of $LaCo_{1-x}Rh_xO_3$ catalysts prepared with different Rh content of (a) x = 0.1, (b) x = 0.2, (c) x = 0.3 and (d) x = 0.4.

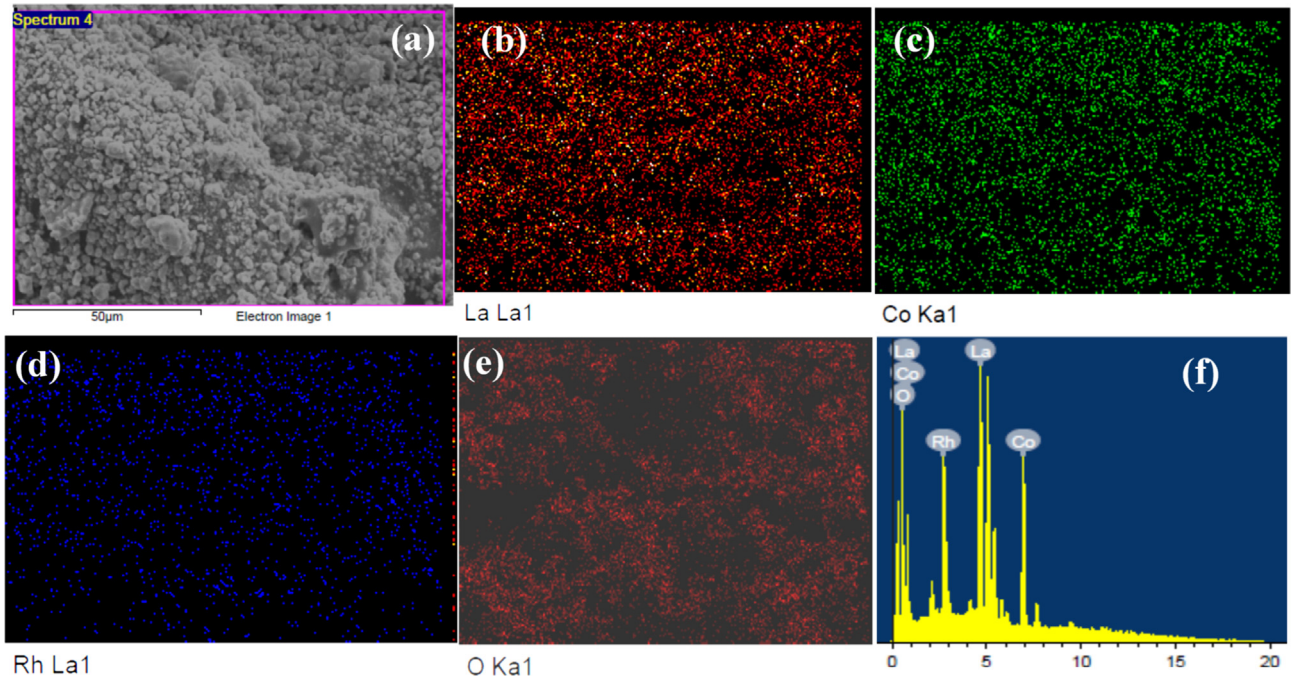


**Fig. 3** EDX elemental maps and composition analysis of $LaCo_{0.7}Rh_{0.3}O_3$ sample, (a) SEM image, (b) La, (c) Co, (d) Rh, (e) O, and (f) EDX histogram of La, Co, Rh, and O elements.

**Table 1** EDX elemental analysis of the as-prepared $LaCo_{1-x}Rh_xO_3$ catalysts.

| Catalyst intended composition | La wt. % (mole ratio) | Co wt. % (mole ratio) | Rh wt. % (mole ratio) | O wt. % (mole ratio) |
|---|---|---|---|---|
| $LaCo_{0.9}Rh_{0.1}O_3$ | 50.06 (1.0) | 20.17 (0.93) | 4.07 (0.10) | 25.17 (4.32) |
| $LaCo_{0.8}Rh_{0.2}O_3$ | 51.34 (1.0) | 17.35 (0.79) | 8.14 (0.21) | 23.17 (3.92) |
| $LaCo_{0.7}Rh_{0.3}O_3$ | 49.01 (1.0) | 14.17 (0.72) | 11.23 (0.31) | 24.86 (4.40) |
| $LaCo_{0.3}Rh_{0.7}O_3$ | 50.36 (1.0) | 6.49 (0.3) | 22.23 (0.685) | 20.93 (3.55) |

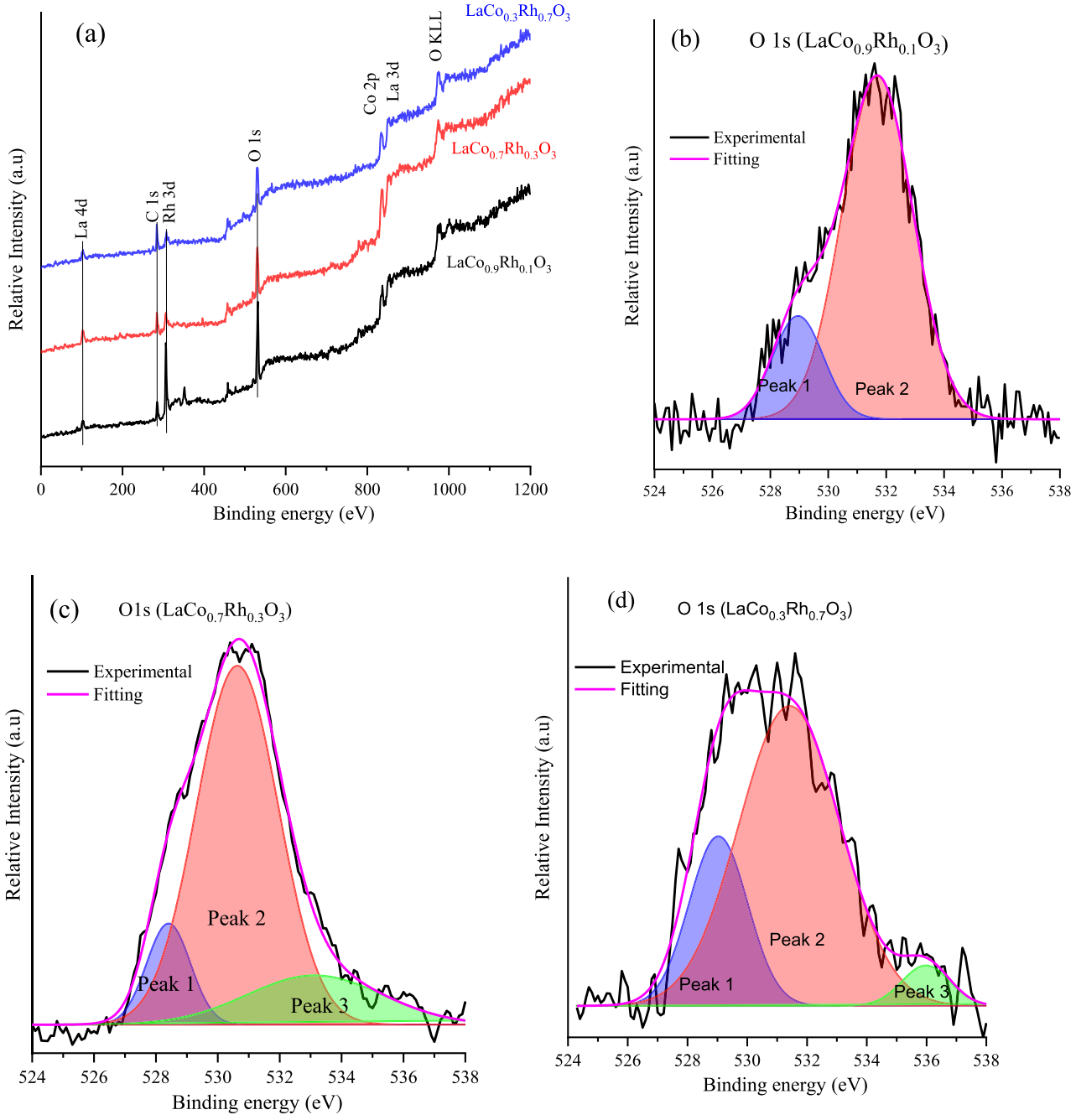


**Fig. 4** Surface and chemical composition of $LaCo_{1-x}Rh_xO_3$ catalysts. (a) Comparative XPS survey spectra of $LaCo_{1-x}Rh_xO_3$ catalysts at x = 0.1, 0.3, and 0.7 and the core-level of O 1s spectra of (b) $LaCo_{0.9}Rh_{0.1}O_3$, (c) $LaCo_{0.7}Rh_{0.3}O_3$, and (d) $LaCo_{0.3}Rh_{0.7}O_3$ catalysts.

**Table 2** XPS spectra analysis of the deconvoluted O 1s peaks of $LaCo_{1-x}Rh_xO_3$ catalysts.

| Catalyst | Peak BE ($O^{2-}$)/ eV | Peak 1 area % | Peak 2 ($O^{1-}$)/ eV | Peak area % | Peak 3 ($O^{chem}$)/ eV | Peak 3 area % | [$O^{1-}$/ $O^{2-}$] | [$O^{1-}$ + $O^{chem}$/ $O^{2-}$] |
|---|---|---|---|---|---|---|---|---|
| $LaCo_{0.9}Rh_{0.1}O_3$ | 528.96 | 17.78 | 531.70 | 82.22 | – | – | 4.62 | 3.25 |
| $LaCo_{0.7}Rh_{0.3}O_3$ | 528.4 | 10.9 | 530.64 | 72.60 | 533.13 | 16.45 | 6.66 | 8.17 |
| $LaCo_{0.3}Rh_{0.7}O_3$ | 529.0 | 23.50 | 531.42 | 71.91 | 535.98 | 4.58 | 3.06 | 3.25 |

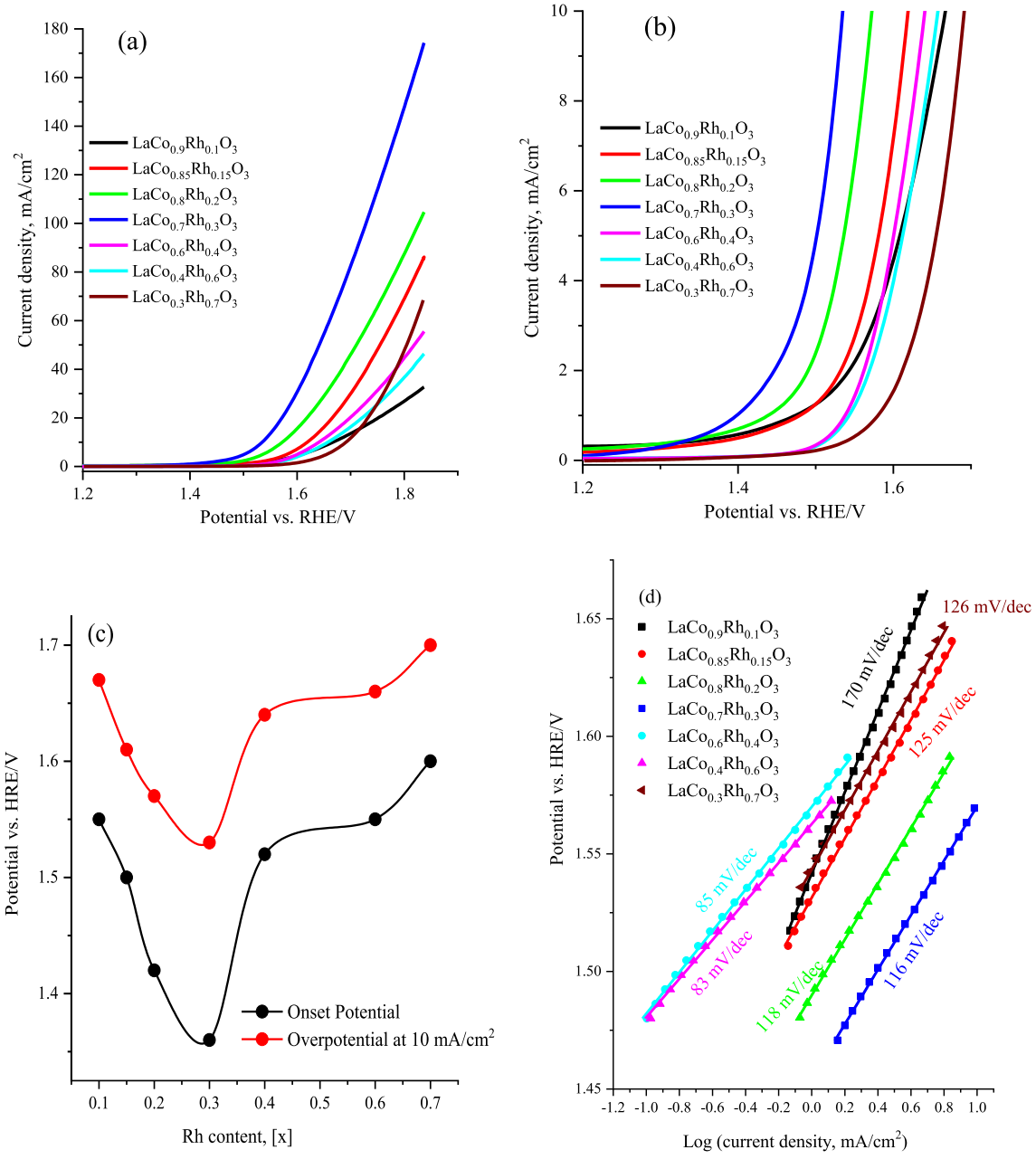


**Fig. 5** (a) linear sweep voltammetry (LSV) within the potential range of the OER at 5 mV/s and in 1.0 M KOH of the Rh substitution $LaCo_{1-x}Rh_xO_3$ catalysts (x = 0.1, 0.15, 0.2, 0.3, 0.4, 0.6, 0.7) loaded carbon paper substrate, (b) magnification of the LSV (a) showing the OER onset potential and the overpotential at 10 mA/cm$^2$, (c) the plot of Rh content (x values) and the onset potential (extracted at 1.0 mA/cm$^2$) and the overpotential required to achieve a current density of 10 mA/cm$^2$ of the $LaCo_{1-x}Rh_xO_3$ catalysts, (d) Tafel plots obtained by fitting the LSV data to the Tafel equation of the Rh substitution $LaCo_{1-x}Rh_xO_3$ catalysts.

rate of lattice oxygen diffusion which contributes to the surface (Pan et al., 2020; Sun et al., 2021). In addition, the deconvoluted XPS core spectra of rhodium (Rh 3d) shown in Fig. S1a revealed the presence of Rh $3d_{5/2}$ and Rh $3d_{3/2}$ levels peaks located at binding energies of 306.26 and 310.24 eV, respectively. Fig. S1b shows the deconvoluted core XPS spectra of the Co 2p zone which compromised multi-peaks that related to the Co 2p3/2 and Co 2p1/2 levels and extended over the 740 to 800 eV binding energy values. The XPS spectra of Co 2p are complex presumably due to the presence of satellite peaks and different cobalt oxidation states ($Co^{2+}$ and $Co^{3+}$) that coordinate to a different number of oxygen atoms.

### *3.2. Electrochemical performance of $LaCo_{1-x}Rh_xO_3$ catalysts towards the OER*

To investigate the role of Rh doping and generated oxygen vacancies on the electrochemical activity of the $LaCo_{1-x}Rh_xO_3$ catalysts towards the electrochemical OER, CV surveys were performed in an $N_2$-saturated 1.0 M KOH solution within the OER potential range. Fig. 5a shows the comparative linear sweep voltammograms (LSV) at 50 mV $s^{-1}$ while Fig. 5b shows a magnified LSV at a current of 10 mA/$cm^2$ for the $LaCo_{1-x}Rh_xO_3$ catalysts with different Rh content in 1.0 M KOH solution. Fig. 5c shows a plot of Rh content (x values) and the onset potential ($\eta_{onset}$, extracted at 1.0 mA/$cm^2$) and the overpotential needed to achieve 10 mA/$cm^2$ ($\eta^2_{10\ mA/cm}$) for the $LaCo_{1-x}Rh_xO_3$ catalysts while Fig. 5d shows the corresponding OER Tafel slopes of the studied $LaCo_{1-x}Rh_xO_3$ catalysts as obtained from LSV data in Fig. 5a. Moreover, Table 3 shows the overall characteristic catalyst electrochemical parameters of the onset potential (($\eta_{onset}$), the overpotential at the current density of 10 mA/$cm^2$ ($\eta^2_{10\ mA/cm}$), and the Tafel slope of the $LaCo_{1-x}Rh_xO_3$ catalysts. The results revealed that the $LaCo_{1-x}Rh_xO_3$ catalyst electrodes exhibit the typical electrochemical features of OER of water electrolysis. Among the studied electrocatalysts, the $LaCo_{0.7}Rh_{0.3}O_3$ electrode with x = 0.3 was the most active electrocatalyst. Fig. 5c shows an inverted volcanic plot where the OER onset potential ($\eta_{onset}$) and similarly the ($\eta^2_{10\ mA/cm}$) gradually decrease as the Rh content increases, reaching minimum values of 1.38 and 1.53 V vs HRE, respectively, at $Rh_x$ = 0.3, indicating the superior intrinsic catalytic activity of the $LaCo_{0.7}Rh_{0.3}O_3$ catalyst towards the OER. The results in Fig. 5 and Table 2 prove that the OER electrocatalytic activity of the $LaCo_{1-x}Rh_xO_3$ electrodes mainly depends on the co-doping level of Rh atoms and the $LaCo_{0.7}Rh_{0.3}O_3$ electrode (x = 0.3) is the most active electrode with an oxygen evolution catalyst mass activity of 290.8 A/$cm^2$ g as measured from the polarization curves in Fig. 5a, which is much higher than those for the other studied electrodes (Table 3).

The water oxidation kinetics of the $LaCo_{1-x}Rh_xO_3$ electrodes were observed by Tafel plots obtained by fitting the LSV data to the Tafel equation (Tüysüz et al., 2013). Fig. 5d shows the Tafel slope of the $LaCo_{1-x}Rh_xO_3$ electrodes during OER their values are also reported in Table 3.We can note that as the Rh content increases, the Tafel slope shifts towards lower values and reach ~ 116 mV/dec for $LaCo_{0.7}Rh_{0.3}O_3$ electrode which indicates which is indicative of the facile surface kinetics and enhanced charge-transfer rate for the OER due to the increased oxygen vacancy content. Moreover, the mass activities of the $LaCo_{1-x}Rh_xO_3$ catalysts at 1.8 V vs HRE presented in Table 3 reveal significant enhancement from 14.50 to 104.20 mA/$cm^2$ g upon the increase of the Rh content (x) from 0.1 to 0.3 respectively. It is worth noting that the OER mass activity and onset potential achieved by the $LaCo_{0.7}Rh_{0.3}O_3$ electrode are higher than those previously reported lanthanum-based perovskite catalysts (Shen et al., 2022; Lu et al., 2019; Dias et al., 2020; Kim et al., 2017).

The charge carrier transfer resistance during the OER for the Rh-substituted $LaCo_{1-x}Rh_xO_3$ catalysts was analyzed by electrochemical impedance spectroscopy (EIS). Fig. 6a shows typical Nyquist plots for $LaCo_{1-x}Rh_xO_3$ supported on a CP electrode in 1.0 M KOH electrolyte at 1.65 V vs HRE. Moreover, the corresponding fitted equivalent circuit is provided in Fig. 6a (inset) which matches the solution resistance ($R_s$), double-layer capacitance ($Q_1$), and charge-transfer resistance ($R_1$). Notably, the results in Fig. 6a revealed the radii of the arc in the impedance plots of $LaCo_{0.7}Rh_{0.3}O_3$ are lower than those of the other electrodes with different Rh contents. Furthermore, the result indicates that the $LaCo_{0.7}Rh_{0.3}O_3$ electrode exhibits faster charge-transfer kinetics and highly effective electrocatalyst for OER. Table 4 reports the impedance parameters of the fitted equivalent circuit and $LaCo_{0.7}Rh_{0.3}O_3$ shows the lowest $R_1$ value of 12.32 O, signifying lower resistance for charge-transfer and, thereby, fast electrode

**Table 3** The electrochemical catalyst parameters of onset potential, overpotential at 10 mA/$cm^{-2}$, Tafel slope, and mass activity of OER for fabricated $LaCo_{1-x}Rh_xO_3$ catalysts.

| Rh ratio (x) | OER onset potential/ V | η OER @10 mA/$cm^2$ | OER Tafel slope mV/dec | Mass activity @1.6 V (A/$cm^2$ g) | Ref. |
|---|---|---|---|---|---|
| 0.1 | 1.55 | 1.67 | 170 | 14.50 | This work |
| 0.15 | 1.50 | 1.67 | 125 | 25.55 | This work |
| 0.2 | 1.42 | 1.57 | 118 | 52.30 | This work |
| 0.3 | 1.38 | 1.53 | 116 | 104.20 | This work |
| 0.4 | 1.52 | 1.64 | 85 | 17.60 | This work |
| 0.6 | 1.54 | 1.66 | 83 | 14.53 | This work |
| 0.7 | 1.59 | 1.70 | 126 | 5.60 | This work |
| $LaCo_{0.7}Rh_{0.3}O_3$ (0.1 M KOH) | 1.50 | 1.58 | 150 | 33.50 | This work |
| $LaCoO_3$ (microparticles) | 1.58 | 1.70 | 92 | ~35.0 | (Shen et al., 2022) |
| $LaCoO_3$ (dense, porous, hollow particles) | (1.58, 1.54, 1.52) | (1.66, 1.61, 1.58) | (76, 74, 72) | (~10.0, ~37.5, ~67.5) | (Kim et al., 2017) |

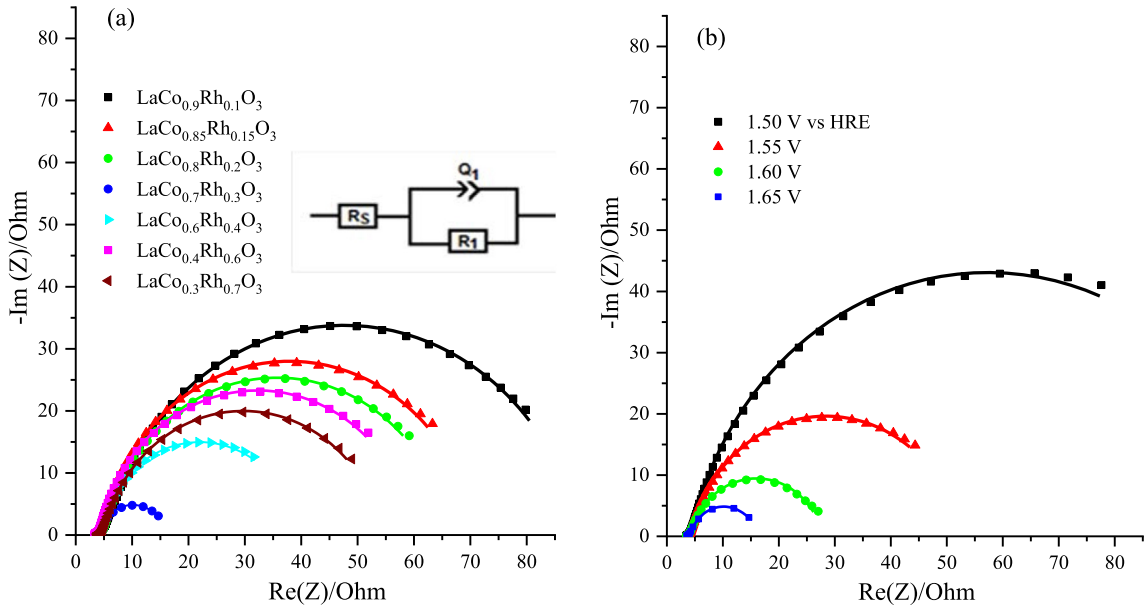


**Fig. 6** (a) EIS Nyquist diagram and equivalent circuit of the $LaCo_{1-x}Rh_xO_3$ catalysts in 1.0 M KOH electrolyte measured at 1.65 V vs HREand within the frequency region of 0.01 to $10^5$ Hz with a 20 mV amplitude. The insets are the fitted equivalent circuit (b) EIS Nyquist plots and equivalent circuit for the $LaCo_{0.7}Rh_{0.3}O_3$ at the different applied potential within the frequency region of 0.01 to $10^5$ Hz and a 20 mV amplitude in 1.0 M KOH. The solid lines are the fitted curves, and the symbols represent the experimental data.

**Table 4** Impedance parameters were obtained from the fitting of the equivalent circuit for $LaCo_{1-x}Rh_xO_3$ catalysts recorded in 1.0 M KOH solution at 1.65 V vs HRE.

| Catalysts | $R_s$(ohm) | $Q_1$ mF.s$^{(a-1)}$ | $R_1$ (ohm) |
|---|---|---|---|
| $LaCo_{0.9}Rh_{0.1}O_3$ | 3.93 | 8.21 | 83.10 |
| $LaCo_{0.8}5Rh_{0.15}O_3$ | 3.36 | 9.28 | 66.38 |
| $LaCo_{0.8}Rh_{0.2}O_3$ | 4.48 | 6.08 | 61.50 |
| $LaCo_{0.7}Rh_{0.3}O_3$ | 3.58 | 2.34 | 12.32 |
| $LaCo_{0.6}Rh_{0.4}O_3$ | 3.93 | 6.02 | 34.96 |
| $LaCo_{0.3}Rh_{0.7}O_3$ | 3.42 | 1.26 | 56.34 |

**Table 5** Impedance parameter values resulting from the equivalent circuit fitting for the spectra of $LaCo_{0.3}Rh_{0.7}O_3$ catalyst at different applied biases in 1.0 M KOH solution.

| Potential (V vs HRE) | $R_s$(ohm) | $Q_1$ mF.s$^{(a-1)}$ | $R_1$ (ohm) |
|---|---|---|---|
| 1.50 | 3.51 | 2.45 | 105.7 |
| 1.55 | 3.57 | 2.40 | 51.65 |
| 1.60 | 3.54 | 4.56 | 23.70 |
| 1.65 | 3.58 | 2.34 | 12.32 |

kinetics, agreeing with its superior intrinsic activity toward OER.

In addition, the resistance for charge transfer of the most active catalyst $LaCo_{0.7}Rh_{0.3}O_3$ was examined at different applied voltages by EIS analysis. Typically, Fig. 6b shows the Nyquist plots acquired for the $LaCo_{0.7}Rh_{0.3}O_3$ catalyst at 20 mV amplitude and from 0.01 to $10^5$ Hz frequency range. The radii of the arc for the $LaCo_{0.7}Rh_{0.3}O_3$ electrode decrease with increasing applied potential from 1.50 to 1.65, demonstrating that the resistance for the charge transfer of the $LaCo_{0.7}Rh_{0.3}O_3$ catalyst decreases with increasing applied potential, showing superior OER features.

Moreover, Table 5 tabulates the EIS parameters of solution resistance ($R_s$), double-layer capacitance ($Q_1$), and charge-transfer resistance ($R_1$) resulting from the equivalent fitted circuit (Fig. 6a inset) at various applied potentials of the $LaCo_{0.3}Rh_{0.7}O_3$ electrode. The results indicated that $R_1$ considerably declined from 105.7 to 12.32 O by increasing the applied potential from 1.51 to 1.64 V, approving the enrichment of the charge transfer and faster OER kinetics at the $LaCo_{0.7}Rh_{0.3}O_3$ catalyst.

The electrocatalytic features of the $LaCo_{0.7}Rh_{0.3}O_3$ electrode during the OER in 1.0 M KOH were further improved by studying the electrolyte concentration, catalyst loading effect, and long-term durability at a predefined current density or constant potential. Fig. S2a (Supporting Information) displays the LSV at 50 mV $s^{-1}$ for $LaCo_{0.3}Rh_{0.7}O_3$/CP electrodes with different catalyst loadings. Moreover, Fig. S2b shows the plot of the relationship of catalyst loading against the potential at 10 mA/cm$^2$ (black line) in addition to the current density attained at 1.8 V vs HRE (red line) for the OER. Apparently, $LaCo_{0.3}Rh_{0.7}O_3$ loading of around 0.3 mg/cm$^2$ was found to give superior OER activity (Fig. S2b) where the minimum potential at 10 mA/cm$^2$ and the highest current density at 1.8 V vs RHE were achieved. Further, Fig. S2c elucidates the LSV profiles at 50 mV/s of 0.3 mg/cm$^2$ $LaCo_{0.7}Rh_{0.3}O_3$ catalyst upon increasing KOH concentration (0.1 – 5.0 M), which revealed a decrease in the onset potential as well as an enhancement of the OER current density at more positive potential. This behavior could be attributed to the Nernst

effect and $OH^-$ ion concentration increment at the catalyst–electrolyte interface respectively which signifies the OER enhancement at $LaCo_{0.3}Rh_{0.7}O_3$ in concentrated alkaline media.

The results in Fig. 7 display the long-term chronoamperometry (current–time) and chronopotentiometry (potential-time) profiles at a predefined applied voltage and current density through the continued OER using the $LaCo_{0.7}Rh_{0.3}O_3$ electrode in 1.0 M KOH solution. The $LaCo_{0.7}Rh_{0.3}O_3$ electrode shows long-term electrochemical durability with a reasonably stable current and potential during the electrochemical water oxidation process (Fig. 7a). Furthermore, the capability of the $LaCo_{0.3}Rh_{0.7}O_3$ electrode to operate at different current densities was investigated (Fig. 7b). The electrodes exhibited a potential of 1.54 V vs RHE to attain a current density of 10 mA/cm$^2$ required for 10 % solar to hydrogen production efficiency, outperforming the benchmarked catalysts prepared by other approaches.

### *3.3. Electrochemical performance of the $LaCo_{1-x}Rh_xO_3$ catalysts for the ORR*

The ORR electrocatalytic features of the $LaCo_{1-x}Rh_xO_3$ catalysts were determined via CV in a 1.0 M KOH solution. Fig. 8a shows the CV for the $LaCo_{0.7}Rh_{0.3}O_3$ (0.3 mg/cm$^2$) catalyst examined in $N_2$– and $O_2$-saturated 1.0 M KOH solutions using a glassy carbon electrode (GC, 3.0 mm diameter). As shown in Fig. 8a, the CV curves display a characteristic ORR peak in the $O_2$-saturated medium, which completely vanishes in the $N_2$-saturated KOH solution. Besides, the onset potential of oxygen reduction is at 0.76 V vs HRE, and a peak current of −0.2 mA/cm$^2$ was obtained, which proves the enhancement of ORR at $LaCo_{0.7}Rh_{0.3}O_3$ catalyst in alkaline solution. In addition, Fig. 8b presents comparative LSV curves for ORR activity acquired using a CP electrode loaded with the $LaCo_{1-x}Rh_xO_3$ catalysts with different Rh contents in a 1.0 M KOH solution. In addition, Fig. 8d and Table 6 summarize the overall characteristic catalyst electrochemical parameters of the ORR onset potential, the overpotential at a current density of 10 mA/cm$^2$, Tafel slope, and ΔE (the potential gap between the OER and ORR onset potentials) of the $LaCo_{1-x}Rh_xO_3$ catalysts. The results show that the $LaCo_{0.7}Rh_{0.3}O_3$ electrode with x = 0.3 is the most effective electrocatalyst for the ORR. The onset potential of ORR, as well as the potential at 10 mA/cm$^2$ ((10 mA/cm$^2$), have shifted to more positive values of 0.73 and 0.64 V vs HRE, respectively, at Rh (x) = 0.3, indicating the superior catalytic activity of the $LaCo_{0.7}Rh_{0.3}O_3$ catalyst towards the ORR. Moreover, the OER/ORR overpotential gap (ΔE) of the $LaCo_{0.7}Rh_{0.3}O_3$ catalyst is about 0.65 V, which is considerably lower than that of the other investigated Rh-doped $LaCo_{1-x}Rh_xO_3$ catalysts. as well as that of the reference analog hybrids.

To verify the ORR catalytic pathways for the $LaCo_{0.7}Rh_{0.3}O_3$ catalyst, we adopted an RRDE technique to screen the formation of hydrogen peroxide species ($H_2O_2$) during the ORR process. Fig. 9a displays the cathodic LSV plots logged at 2000 rpm in $O_2$-saturated electrolyte at $LaCo_{0.7}Rh_{0.3}O_3$ catalyst using the disk (lower part) and ring electrodes (upper part). For both the disk and ring electrodes, the ORR onset potentials commence at 0.7 V vs HRE, and the wave of 0.2 and 0.025 mA cm$^{-2}$ is achieved at 0.54 V vs HRE, revealing the oxygen reduction at disc $LaCo_{0.7}Rh_{0.3}O_3$ and peroxide species oxidation at platinum ring electrodes respectively.

Through calculation, Fig. 9b displays the average electron transfer number (n) for the $LaCo_{0.7}Rh_{0.3}O_3$ electrode in the potential range from 0.7 to 0.2 V HRE, which was 3.9, indicating that the ORR involves a four-electron pathway for the $LaCo_{0.7}Rh_{0.3}O_3$ electrode. Moreover, the $H_2O_2$ production rate calculated from the ring current at the $LaCo_{0.7}Rh_{0.3}O_3$ electrode was around 5–10 % in the potential range of 0.7–0.2 VRHE (Fig. 9b), which indicates the minimum production

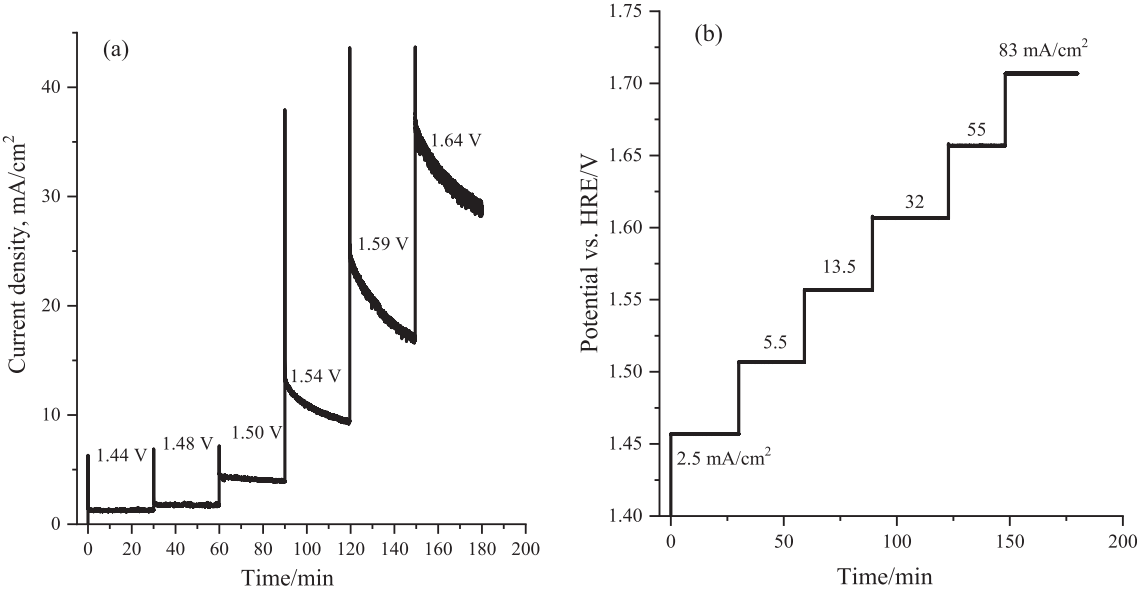


**Fig. 7** Electrochemical durability tests of the $LaCo_{0.7}Rh_{0.3}O_3$ catalyst (loading 0.3 mg/cm$^2$) during OER in 1.0 M KOH, (a) Chronoamperometric response at different applied voltage steps, and (b) chronopotentiometry response of the catalyst at a different applied current density during continued oxygen evolution reaction.

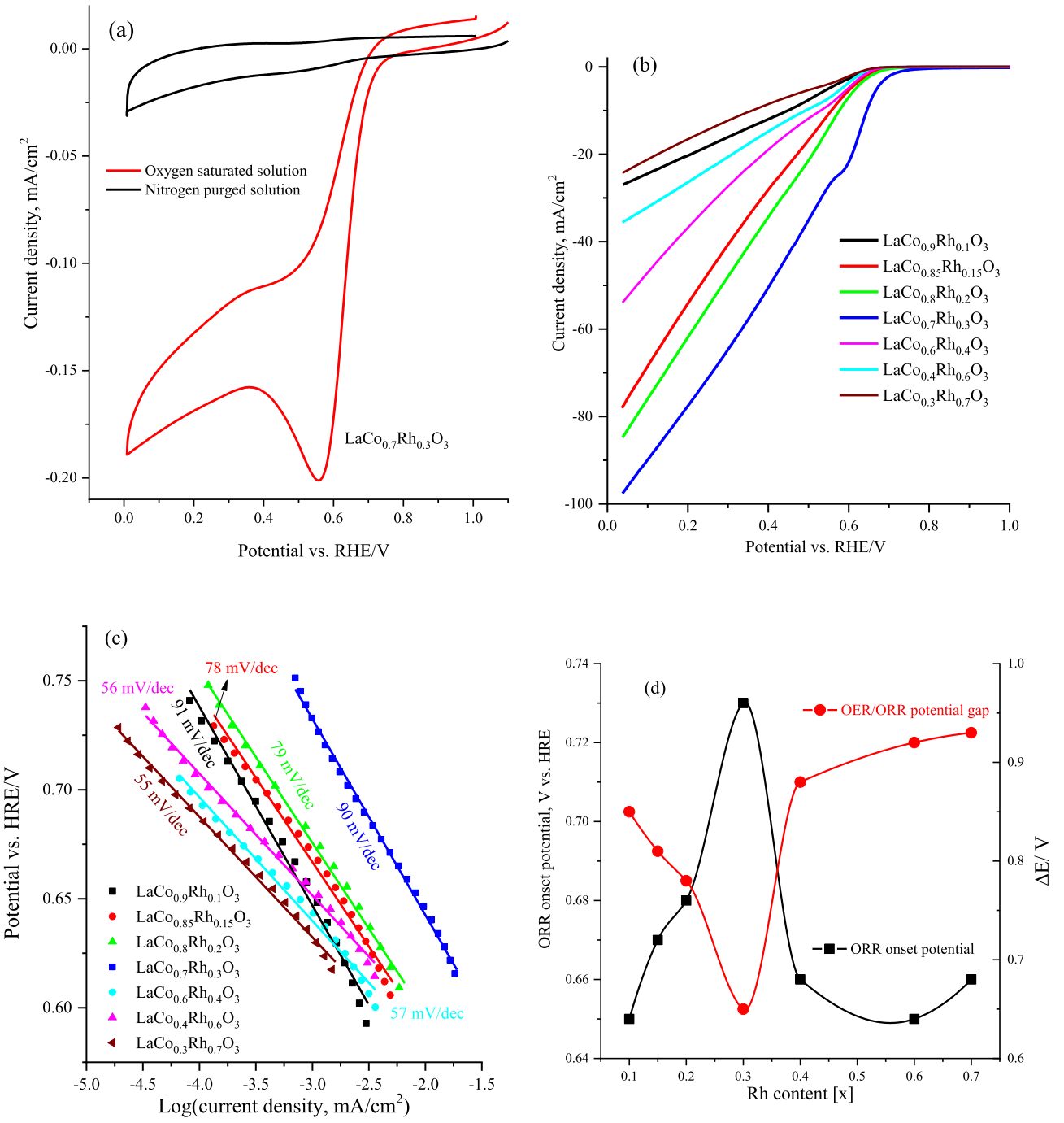


**Fig. 8** (a) cyclic voltammetry curves at a scan rate of 10 mV/s of $LaCo_{0.7}Rh_{0.3}O_3$ catalyst loaded on glassy carbon electrode in 1.0 M KOH solution saturated with $N_2$ (black line) or oxygen (red line) at a scan rate of 10 mV/s,(b) cathodic-going linear sweep voltammograms within the ORR potential window at 10 mV/s of $LaCo_{1-x}Rh_xO_3$ catalysts loaded on carbon paper electrode in 1.0 M KOH solution, (c) the corresponding Tafel plots obtained by fitting the LSV data to the Tafel equation of the Rh doped $LaCo_{1-x}Rh_xO_3$ catalysts, (d) plot of the relationship of the Rh content and ORR onset potential and OER/ORR potential gap.

rate of hydrogen peroxide and confirms that a high selective $4e^-$ ORR process was achieved.

Finally, Fig. 9c and 9d show the long-term stability of the $LaCo_{0.7}Rh_{0.3}O_3$ electrode towards the ORR as evaluated through chronoamperometric/chronopotentiometry measurements in $O_2$-saturated 1.0 M KOH solution. The $LaCo_{0.3}Rh_{0.7}O_3$ catalyst exhibited stable behavior during the ORR, with no substantial change of the measured potential or current density throughout the measurement for up to 3 h, as shown in Fig. 9c and 9d. The highest current density of 92 mA/cm$^2$ was achieved for $LaCo_{0.7}Rh_{0.3}O_3$ with 0.30 mg/cm$^2$ loading at 0.4 V vs HRE.

**Table 6** The electrochemical catalyst parameters of onset potential, overpotential at 10 mA/cm$^{-2}$, Tafel slope, and mass activity of ORR for fabricated $LaCo_{1-x}Rh_xO_3$ catalysts.

| Rh ratio (x) | ORR onset potential/ V | η ORR at 10 mA/cm$^2$ | ORR Tafel slope mV/dec | ΔE (OER-ORR)/V |
|---|---|---|---|---|
| 0.1 | 0.65 | – | 91 | 0.85 |
| 0.15 | 0.67 | 0.56 | 78 | 0.81 |
| 0.2 | 0.68 | 0.57 | 79 | 0.78 |
| 0.3 | 0.73 | 0.64 | 90 | 0.65 |
| 0.4 | 0.66 | 0.53 | 57 | 0.88 |
| 0.6 | 0.65 | 0.49 | 56 | 0.92 |
| 0.7 | 0.66 | – | 55 | 0.93 |

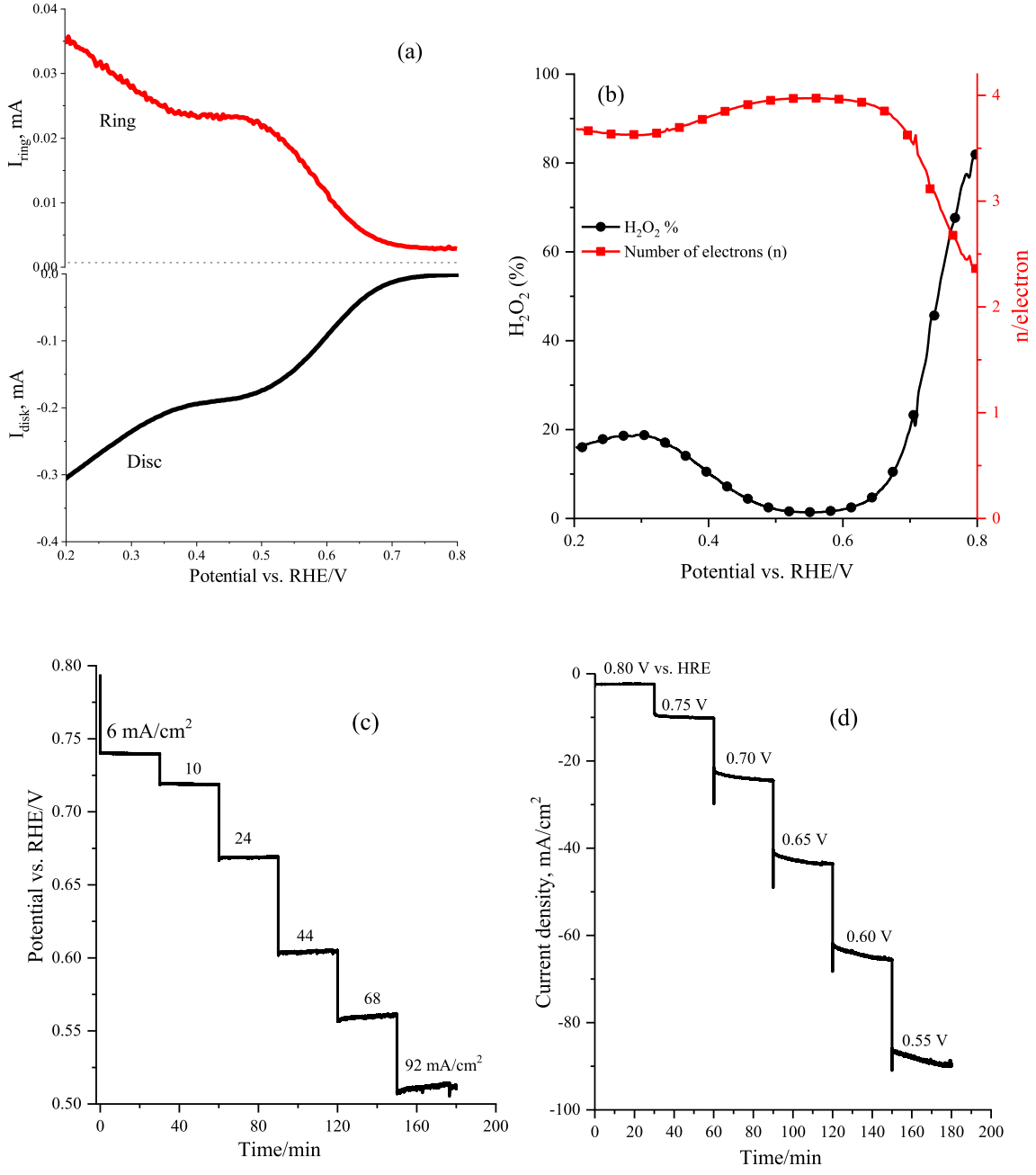


**Fig. 9** (a) Rotating ring-disc electrode (RRDE) polarization curves of $LaCo_{0.7}Rh_{0.3}O_3$ electrode at 2000 rpm in $O_2$ saturated medium with the ring current (upper region), disc current (lower region), and current corresponding to hydrogen peroxide obtained from the ring current, (b) the corresponding average electron transfer number (n) and $H_2O_2$ production rate as a function of the applied potential,(c) chronopotentiometry at different applied current densities, and (d) chronoamperometry at the different applied potential for the$LaCo_{0.7}Rh_{0.3}O_3$ electrode in 1.0 M KOH electrolyte.

## 4. Conclusions

We have validated the fabrication of highly efficient bifunctional OER/ORR catalysts of rhodium-doped $LaCo_{1-x}Rh_xO_3$ (LCRO, $0.1 \leq x \leq 0.70$) perovskite-based oxides via solid-state reactions. A range of characterization methods revealed the effect of the Rh doping level on the $LaCo_{1-x}Rh_xO_3$ surface morphology, oxygen deficiencies, and electrocatalytic activities of the studied $LaCo_{1-x}Rh_xO_3$ catalysts towards the OER and ORR in alkaline solution. It was established that the $LaCo_{0.7}Rh_{0.3}O_3$ hybrid with $x \sim 0.3$ doping is one of the rare and highly active bifunctional electrocatalysts for OER/ORR. The $LaCo_{0.7}Rh_{0.3}O_3$ catalysts with $x \sim 0.3$ doping revealed exceptional OER/ORR bifunctional electrocatalytic activities, low onset potentials (1.38 V OER and 0.73 V ORR), an efficient four-electron ORR pathway, and a small OER/ORR onset potential gap ($\Delta E$) of 0.65 V, which is considerably superior to the reported lanthanum-based perovskite catalysts. The enhanced electrochemical OER and ORR activities of the $LaCo_{0.7}Rh_{0.3}O_3$ catalyst over the other Rh doping ratios can be rationalized due to the lattice expansion, higher oxygen vacancies, and enhanced B—O bond covalency, which increases the active sites and the electrical conductivity of the $LaCo_{1-x}Rh_xO_3$ catalysts.

## Declaration of Competing Interest

The authors declare that they have no known competing financial interests or personal relationships that could have appeared to influence the work reported in this paper.

## Acknowledgments

This project was funded by the National Plan for Science, Technology, and Innovation (MAARIFAH), King Abdelaziz City for Science and Technology (KACST), Kingdom of Saudi Arabia, Award Number 13-ENE-1227-02.

## Appendix A. Supplementary material

Supplementary data to this article can be found online at https://doi.org/10.1016/j.arabjc.2022.104256.

## References

Bockris, J.O., Otagawa, T., 1984. The electrocatalysis of oxygen evolution on perovskites. J. Electrochem. Soc. 131 (2), 290–302. https://doi.org/10.1149/1.2115565.

Celorrio, V., Dann, E., Calvillo, L., Morgan, D.J., Hall, S.R., Fermin, D.J., 2015. Oxygen reduction at carbon-supported lanthanides: the role of the B-site. ChemElectroChem 3, 283–291.

Chang, H., Bjørgum, E., Mihai, O., Yang, J., Lein, H.L., Grande, T., Raaen, S., Zhu, Y.-A., Holmen, A., Chen, D., 2020. Effects of oxygen mobility in la–Fe-based perovskites on the catalytic activity and selectivity of methane oxidation. ACS Catal. 10 (6), 3707–3719. https://doi.org/10.1021/acscatal.9b05154.

Chen, Z., Higgins, D., Yu, A., Zhang, L., Zhang, J., 2011. A review on non-precious metal electrocatalysts for PEM fuel cells. Energy Environ. Sci. 4 (9), 3167–3192. https://doi.org/10.1039/c0ee00558d.

Cheng, F., Zhang, T., Zhang, Y., Du, J., Han, X., Chen, J., 2013. Enhancing electrocatalytic oxygen reduction on $MnO_2$ with vacancies. Angew. Chem. 125 (9), 2534–2537. https://doi.org/10.1002/ange.201208582.

Cui, B., Liu, C., Zhang, J., Lu, J., Liu, S., Chen, F., Zhou, W., Qian, G., Wang, Z., Deng, Y., Chen, Y., Hu, W., 2021. Waste to wealth: Defect-rich Ni-incorporated spent LiFePO4 for efficient oxygen evolution reaction. Sci China Mater 64 (11), 2710–2718.

Debe, M.K., 2012. Electrocatalyst approaches and challenges for automotive fuel cells. Nature 486 (7401), 43–51. https://doi.org/10.1038/nature11115.

Dias, J.A., Andrade, M.A.S., Santos, H.L.S., Morelli, M.R., Mascaro, L.H., 2020. Lanthanum-based perovskites for catalytic oxygen evolution reaction. ChemElectroChem 7 (15), 3173–3192. https://doi.org/10.1002/celc.202000451.

Dong, F., Li, L., Kong, Z., Xu, X., Zhang, Y., Gao, Z., Dongyang, B., Ni, M., Liu, Q., Lin, Z., 2021. Materials engineering in perovskite for optimized oxygen evolution electrocatalysis in alkaline conditions. Small 17 (2), e2006638.

Dou, S., Xu, J., Cui, X., Liu, W., Zhang, Z., Deng, Y., Hu, W., Chen, Y., 2020. [High-Temperature Shock Enabled Nanomanufacturing for Energy-Related Applications. Adv. Energy Mater. 10, 2001331.

Dupin, J., Gonbeau, D., Vinatier, P., Levasseur, A., 2000. Systematic XPS studies of metal oxides, hydroxides, and peroxides. PCCP 2 (6), 1319–1324. https://doi.org/10.1039/a908800h.

Feng, S., Liu, C., Chai, Z., Li, Q., Xu, D., 2018. Cobalt-based hydroxide nanoparticles@N-doping carbonic frameworks core-shell structures as highly efficient bifunctional electrocatalysts for oxygen evolution and oxygen reduction reactions. Nano Res. 11 (3), 1482–1489. https://doi.org/10.1007/s12274-017-1765-2.

Ghanem, M.A., Arunachalam, P., Almayouf, A.M., Weller, M.T., 2016. Efficient bi-functional electrocatalysts of strontium iron oxyhalides for oxygen evolution and reduction reactions in alkaline media. J. Electrochem. Soc. 163 (6), H450–H458. https://doi.org/10.1149/2.1171606jes.

Ghanem, M.A., Amer, M.S., Al-Mayouf, A.M., Arunachalam, P., Weller, M.T., 2021. Halide-doping effect of strontium cobalt oxide electrocatalyst and the induced activity for oxygen evolution in an alkaline solution. Catalysts 11 (11). https://doi.org/10.3390/catal11111408.

Harris, J., 1970. Low-cost oxygen electrode material. Nature 226 (5248), 848–849. https://doi.org/10.1038/226848a0.

Kim, J., Chen, X., Shih, P.-C., Yang, H., 2017. Porous Perovskite-Type Lanthanum Cobaltite as Electrocatalysts toward Oxygen Evolution Reaction. ACS Sustainable Chem. Eng. 5, 10910–10917. https://doi.org/10.1021/acssuschemeng.7b02815.

Kim, B.J., Fabbri, E., Abbott, D.F., Cheng, X., Clark, A.H., Nachtegaal, M., Borlaf, M., Castelli, I.E., Graule, T., Schmidt, T.J., 2019. Functional role of Fe-doping in co-based perovskite oxide catalysts for oxygen evolution reaction. J. American Chem. Soc. 141 (13), 5231–5240. https://doi.org/10.1021/jacs.8b12101.

Kobussen, A.G.C., Broers, G.H.J., 1981. The oxygen evolution on $La_{0.5}Ba_{0.5}CoO_3$. J. Electroanal. Chem. Interfacial Electrochem. 126 (1–3), 221–240. https://doi.org/10.1016/S0022-0728(81)80430-5.

Lee, J.E., Jeon, K.-J., Show, P.L., Lee, I.H., Jung, S.-C., Choi, Y.J., Rhee, G.H., Lin, K.-Y.-A., Park, Y.-K., 2022. Mini review on $H_2$ production from electrochemical water splitting according to special nanostructured morphology of electrocatalysts. Fuel 308,. https://doi.org/10.1016/j.fuel.2021.122048 122048.

Lemoine, K., Lhoste, J., Hémon-Ribaud, A., Heidary, N., Maisonneuve, V., Guiet, A., Kornienko, N., 2019. Investigation of mixed-metal (oxy)fluorides as a new class of water oxidation electrocatalysts. Chem. Sci. 10 (40), 9209–9218. https://doi.org/10.1039/c9sc04027g.

Liu, Y., Wang, W., Xu, X., Marcel Veder, J.P.M., Shao, Z., 2019. Recent advances in anion-doped metal oxides for catalytic applications. J. Mater. Chem. A 7 (13), 7280–7300. https://doi.org/10.1039/C8TA09913H.

Lu, Y., Ma, A., Yu, Y., Tan, R., Liu, C., Zhang, P., Liu, D., Gui, J., 2019. Engineering oxygen vacancies into $LaCoO_3$ perovskite for efficient electrocatalytic oxygen evolution. ACS Sustainable Chem. Eng. 7 (3), 2906–2910. https://doi.org/10.1021/acssuschemeng.8b05717.

Marini, S., Salvi, P., Nelli, P., Pesenti, R., Villa, M., Berrettoni, M., Zangari, G., Kiros, Y., 2012. Advanced alkaline water electrolysis.

Electrochim. Acta 82, 384–391. https://doi.org/10.1016/j.electacta.2012.05.011.

Matsumoto, Y., Sato, E., 1980. Electrochemical properties of the single crystal $La_{0.7}Pb_{0.3}MnO_3$ electrode. Electrochim. Acta 25 (5), 585–589. https://doi.org/10.1016/0013-4686(80)87061-7.

Matsumoto, Y., Yoneyama, H., Tamura, H., 1977. Catalytic activity for electrochemical reduction of oxygen of lanthanum nickel oxide and related oxides. J. Electroanal. Chem. Interfacial Electrochem. 79 (2), 319–326. https://doi.org/10.1016/S0022-0728(77)80453-1.

Mefford, J.T., Rong, X., Abakumov, A.M., Hardin, W.G., Dai, S., Kolpak, A.M., Johnston, K.P., Stevenson, K.J., 2016. Water electrolysis on La(1–x)Sr(x)CoO(3-δ) perovskite electrocatalysts. Nat. Commun. 7, 11053. https://doi.org/10.1038/ncomms11053.

Pan, Y., Xu, X., Zhong, Y., Ge, L., Chen, Y., Veder, J.-P.-M., Guan, D., O'Hayre, R., Li, M., Wang, G., Wang, H., Zhou, W., Shao, Z., 2020. Direct evidence of boosted oxygen evolution over perovskite by enhanced lattice oxygen participation. Nat. Commun. 11 (1), 2002. https://doi.org/10.1038/s41467-020-15873-x.

Petrie, J.R., Cooper, V.R., Freeland, J.W., Meyer, T.L., Zhang, Z., Lutterman, D.A., Lee, H.N., 2016. Enhanced bifunctional oxygen catalysis in strained $LaNiO_3$ perovskites. J. Am. Chem. Soc. 138 (8), 2488–2491. https://doi.org/10.1021/jacs.5b11713.

Shahid, M.M., Rameshkumar, P., Basirun, W.J., Juan, J.C., Huang, N.M., 2017. Cobalt oxide nanocubes interleaved reduced graphene oxide as an efficient electrocatalyst for oxygen reduction reaction in an alkaline medium. Electrochim. Acta 237, 61–68. https://doi.org/10.1016/j.electacta.2017.03.088.

Shen, Z., Qu, M., Shi, J., Oropeza, F.E., de la Peña O'Shea, V.A., Gorni, G., Tian, C.M., Hofmann, J.P., Cheng, J., Li, J., Zhang, K. H.L., 2022. Correlating the electronic structure of perovskite $La_{1-x}Sr_xCoO_3$ with activity for the oxygen evolution reaction: The critical role of Co 3-d hole state. J. Energy Chem. 65, 637–645. https://doi.org/10.1016/j.jechem.2021.06.032.

Sun, J., Du, L., Sun, B., Han, G., Ma, Y., Wang, J., Huo, H., Zuo, P., Du, C., Yin, G., 2021. A bifunctional perovskite oxide catalyst: The triggered oxygen reduction/evolution electrocatalysis by moderated Mn-Ni co-doping. J. Energy Chem. 54, 217–224. https://doi.org/10.1016/j.jechem.2020.05.064.

Suntivich, J., May, K.J., Gasteiger, H.A., Goodenough, J.B., Shao-Horn, Y., 2011. A perovskite oxide optimized for oxygen evolution catalysis from molecular orbital principles. Science 334 (6061), 1383–1385. https://doi.org/10.1126/science.1212858.

Tanaka, H., Misono, M., 2001. Advances in designing perovskite catalysts. Curr. Opin. Solid State Mater. Sci. 5 (5), 381–387. https://doi.org/10.1016/S1359-0286(01)00035-3.

Tüysüz, H., Hwang, Y.J., Khan, S.B., Asiri, A.M., Yang, P., 2013. Mesoporous $Co_3O_4$ as an electrocatalyst for water oxidation. Nano Res. 6 (1), 47–54. https://doi.org/10.1007/s12274-012-0280-8.

Wang, J., Cui, W., Liu, Q., Xing, Z., Asiri, A.M., Sun, X., 2016. Recent progress in cobalt-based heterogeneous catalysts for electrochemical water splitting. Adv. Mater. 28 (2), 215–230. https://doi.org/10.1002/adma.201502696.

Wu, G., More, K.L., Xu, P., Wang, H.L., Ferrandon, M., Kropf, A.J., Myers, D.J., Ma, S., Johnston, C.M., Zelenay, P., 2013. A carbon-nanotube-supported graphene-rich non-precious metal oxygen reduction catalyst with enhanced performance durability. Chem. Commun. 49 (32), 3291–3293. https://doi.org/10.1039/c3cc39121c.

Xia, W., Mahmood, A., Liang, Z., Zou, R., Guo, S., 2016. Earth-abundant nanomaterials for oxygen reduction. Angew. Chem. 55 (8), 2650–2676. https://doi.org/10.1002/anie.201504830.

Xu, X., Pan, Y., Zhong, Y., Ran, R., Shao, Z., 2020. Ruddlesden-Popper perovskites in electrocatalysis. Mater. Horizons 7 (10), 2519–2565. https://doi.org/10.1039/D0MH00477D.

Zhang, L., Sun, W., Xu, C., Ren, R., Yang, X., Qiao, J., Wang, Z., Sun, K., 2020. Attenuating a metal-oxygen bond of a double perovskite oxide: Via anion doping to enhance its catalytic activity for the oxygen reduction reaction. J. Mater. Chem. A 8 (28), 14091–14098. https://doi.org/10.1039/D0TA04820H.

Zhu, H., Zhang, P., Dai, S., 2015. Recent Advances of lanthanum-based perovskite oxides for catalysis. ACS Catal. 5 (11), 6370–6385. https://doi.org/10.1021/acscatal.5b01667.

Zhu, Y., Zhou, W., Yu, J., Chen, Y., Liu, M., Shao, Z., 2016. Enhancing electrocatalytic activity of perovskite oxides by tuning cation deficiency for oxygen reduction and evolution reactions. Chem. Mater. 28 (6), 1691–1697. https://doi.org/10.1021/acs.chemmater.5b04457.